3D-Printed Gradient-Index Phononic Crystal Lens for Underwater Acoustic Wave Focusing

Ahmed Allam⊙,* Karim Sabra⊙, and Alper Erturk⊙

G. W. Woodruff School of Mechanical Engineering, Georgia Institute of Technology, Atlanta, Georgia 30332, USA

A 3D-printed gradient-index phononic crystal structure based on air inclusions in a polymer is introduced to manipulate underwater acoustic waves. The proposed approach enables a simple configuration without heavy inclusions or geometrically complex unit cells to create the required refractive-index profile and focus incident plane waves propagating in a known direction. Based on the band-structure analysis, a gradient-index lens is designed, fabricated, and tested, yielding an excellent agreement between the experimental results and finite-element simulations of underwater acoustic wave focusing. The proposed concept and the resulting lens design can find applications spanning from power enhancement in acoustic energy transfer and harvesting to signal enhancement in sensing and imaging.

I. INTRODUCTION

Gradient-index phononic crystals (GRIN PCs) allow for engineered control of wave propagation beyond what could be achieved using traditional materials. Their effective refractive-index profile can be varied in space by gradually adjusting the lattice structure of the material, thereby steering the direction of propagating waves. Since the effective acoustic impedance usually follows the gradual variation of the refractive index, any reflections that might arise from the steering process are minimized. Different designs for gradient-based and gradient-index materials have been suggested to guide [1,2], focus [3–9], compress [10], absorb [11–13], transmit [14], and retroreflect [15] elastic and acoustic waves, in addition to other applications such as realizing acoustic black holes [16] and asymmetric transmission [17]. Practical realizations of GRIN PCs have focused on 2D devices as in Lamb [18,19] and Rayleigh [20,21] waves. Other realizations involved 2.5D approaches in which the variation of the refractive index occurs in a single plane [22–27].

For underwater acoustic applications, metals are commonly used to construct PCs [5,27–31]. Since manufacturing metals into complex 3D structures is a challenging task, most of the literature has been limited to 2.5D realizations in the form of ordered metallic rods or shells. Additive manufacturing presents a viable approach for fabricating ordered 3D structures; however, 3D printing complex metallic structures is still a challenging task [32].

In-air realization of acoustic GRIN PCs has been recently reported for sonic frequencies [33]. The large impedance contrast between 3D-printed polymers and air

was used to achieve the gradient-index variation required to enable a GRIN PC Luneburg lens. The same approach, however, cannot be easily applied to GRIN PCs for underwater applications, since the impedance contrast between polymers and water is relatively small.

In this work, we introduce a simple structure and design approach for GRIN PCs that allow for the manipulation of underwater acoustic waves. The unit cell of the PC consists of trapped air inclusions in a 3D-printed polylactic acid (PLA) elastic matrix as shown in the inset of Fig. 1(a). The PLA polymer acts as the background medium allowing for a close impedance matching to water while air acts as an impedance contrasting inclusion. This allows for the construction of a simple lightweight PC compared to other common PCs with dense metallic inclusions. The shape of the inclusion is chosen to facilitate its 3D printing via the commonly employed fusion deposition modeling (FDM) process without difficulty [34].

II. UNIT CELL ANALYSIS AND REFRACTIVE INDEX TAILORING

Using an elastic material as the lens background material introduces additional complexity as compared to fluid background of in-air PC lens realizations [33]. First, as shown in Fig. 1(a), two modes of propagation exist in the elastic domain (pressure and shear waves) and thus both modes should be considered when analyzing wave propagation in the PC domain. To simplify the analysis, shear waves (S waves) in the PC are neglected assuming incident acoustic waves in water are mainly coupled to pressure waves (P waves) in the PC domain for the configurations explored in this study. Secondly, the lattice periodicity of the PC, as well as the inclusion size
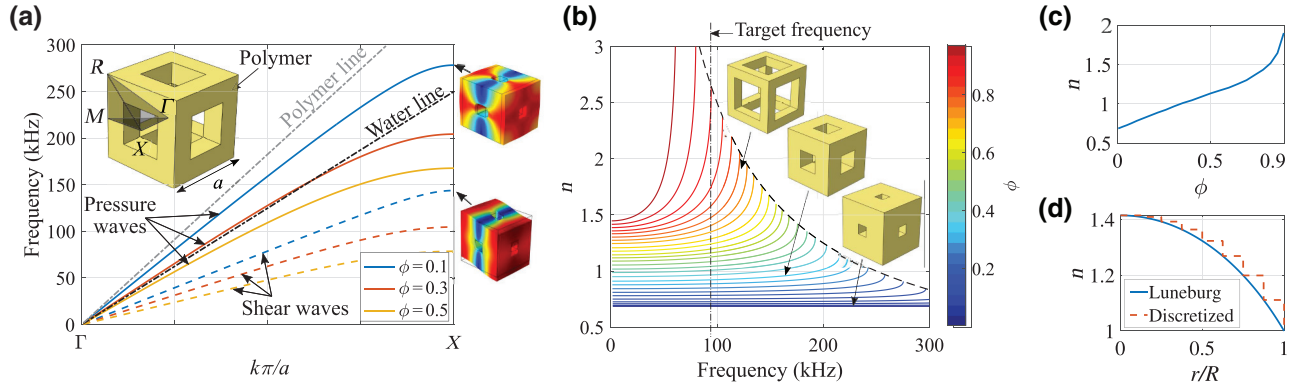

FIG. 1. (a) Band structure of the proposed PC for different filling fractions (ϕ) of air volume per unit cell volume (propagation modes of different branches are shown as insets). (b) Frequency dependence of the PC refractive index for different filling fractions. (c) Dependence of the PC refractive index on the filling fraction at the target frequency of 100 kHz. (d) Refractive-index profile for a continuous Luneburg lens and the discretized GRIN PC implementation. Simulations are for waves propagating in the ΓX direction.

and shape, introduces anisotropy (hence directional dependence) in the effective properties of the PC. The resulting anisotropy is more significant in an elastic background compared to a fluid background, which is isotropic by nature and less sensitive to inclusion shape and periodicity. In the following analysis, we only consider waves propagating in the ΓX direction to characterize the effective properties of the crystal, in an effort to demonstrate the focusing of plane waves propagating in a known direction (omnidirectional implementation would require a more complex unit-cell geometry and fabrication challenge).

An elastic finite-element model (FEM) of the PC unit cell with periodic boundary conditions is used to obtain the band structure shown in Fig. 1(a). The material properties of 3D-printed PLA used in the FEM are obtained experimentally since they usually differ from standard PLA properties depending on the 3D-printing process parameters. In order to identify the actual material properties of the printed structure, homogeneous slender-bar samples are printed using the same 3D-printing process parameters as the PC. The first few axial vibration modes of those samples are employed to estimate the elastic modulus and loss by using the approach detailed in Ref. [35]. The identified properties of the 3D-printed PLA are as follows: Young's modulus $E = 3200$ MPa, density $\rho = 1250$ kg/m^3, Poisson's ratio $\nu = 0.36$, P-wave speed $c_p = 2194$ m/s, S-wave speed $c_s = 1026$ m/s, and structural loss factor $\eta = 0.02$. Furthermore, due to the large impedance mismatch between PLA and air, the inclusions are modeled as free boundary conditions to the elastic domain. While acoustic propagation modes exist in the air inclusions, these modes are weakly coupled to the elastic domain (and to water outside the PC), due to the large impedance mismatch, and do not contribute to the pressure-wave propagation in the PC (confirmed with simulations not shown here).

Figure 1(a) is obtained for a unit cell with periodicity $a = 3$ mm for different filling fractions ϕ defined as the volume of air inclusion to the total volume of the cell. The effective phase velocity of P waves $\tilde{c}_p$ and S waves $\tilde{c}_s$ are given by the relation $\tilde{c}_{p,s} = (2\pi f)/k_{p,s}$, where f is the frequency in Hz and $k_{p,s}$ is the wave number corresponding to the propagation mode. The refractive index of the PC with respect to water is defined as $n = c_w/c_p$, where c_w is the speed of sound in water. When the filling fraction of the air inclusions in the PC is increased, the effective P-wave velocity $\tilde{c}_p$ decreases, i.e., the refractive index of the PC increases. The dependence of the PC refractive index on the frequency is shown in Fig. 1(b) for different filling fractions. The refractive-index profile is relatively flat at lower frequencies and increases rapidly as the frequency approaches the Bragg bandgap of the PC marked by the dashed line. As the filling fraction increases, the bandgap shifts to lower frequencies. As a result, the refractive-index profile becomes steeper and hence less broadband. A target frequency of $f = 100$ kHz is selected so that a range of ϕ can be used to set the refractive index of the PC from $n = 0.7$ (for $\phi = 0$) to $n = 1.9$ (for $\phi = 0.9$) as shown in Fig. 1(c).

III. PC LENS DESIGN

The proposed PC is used to design and fabricate a 3D GRIN PC lens based on the Luneburg lens profile [Fig. 1(d)]: $n = \sqrt{2 - r^2/R^2}$, where r is the distance from the center of the lens, and $R = 24$ mm is the radius of the lens, which consists of 8 unit cells in the radial direction (Luneburg profile is normally omnidirectional, although this work explores the focusing of waves propagating in a single known direction as mentioned previously). In order to reduce the effects of discretization, the air
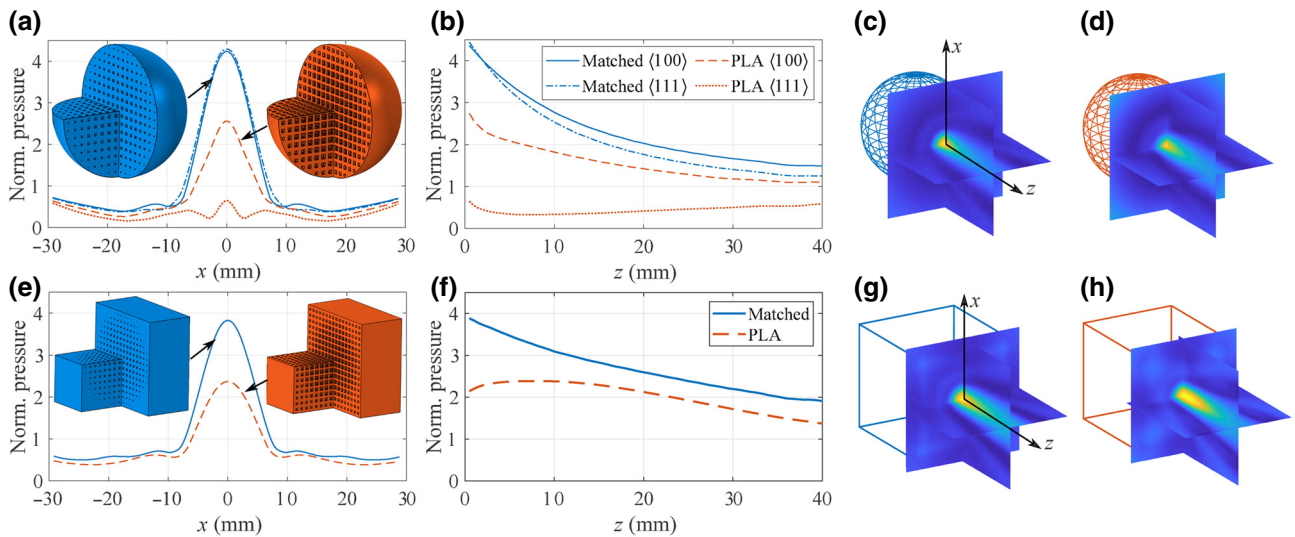
FIG. 2. Normalized pressure field in the focus region of (a)–(d) sphere-shaped lens design and (e)–(h) cube-shaped lens design. The pressure is shown in the propagation (z) direction and the focal plane (x direction). Two different materials for the lens are considered: an elastic material matched to water ($c_p = 1500$ m/s, $c_s = 700$ m/s) shown in solid blue and PLA shown in dashed red. For the sphere lens, the pressure field for waves incident in the $\Gamma X \langle 100 \rangle$ direction are compared to $\Gamma R \langle 111 \rangle$ incidence. Cross sections of the peak pressure-field distributions behind the lenses (i.e., in the focus region) are shown for the matched material (c&g) and PLA (d&h). The internal structures of the lens designs are shown in the insets of (a),(e).

inclusions are tapered to introduce a gradient in the filling fraction between neighboring cells. The performance of the lens is simulated using a coupled elastic-acoustic FEM implemented using COMSOL Multiphysics. The lens is placed in water that is modeled as an acoustic domain with $\rho_w = 1000$ kg/m³ and $c_w = 1500$ m/s. Radiation boundary conditions are applied to the external boundary of the acoustic domain, and both elastic and acoustic domains are discretized so that there are at least seven elements per wavelength at the highest excitation frequency. A Gaussian acoustic plane wave with a center frequency of 100 kHz and bandwidth of 30 kHz is provided as the excitation through one of the acoustic domain boundaries and time-domain response of the lens is computed.

An ideal 3D implementation of the Luneburg lens would be of spherical shape; however, since the lens background is an elastic domain, the shape of the interface between the lens and water will affect its performance due to mode conversion between pressure and shear waves. The interface domain will also have a strong effect on how well incident acoustic waves in water couple to P-waves inside the lens. In addition to the common spherical shape for Luneburg lens, a cube-shaped lens is constructed by setting $\tilde{c}_p$ of the unit cells outside the spherical profile to match c_w. The cube shape provides a flat interface with incident plane waves and thus would provide better coupling to P waves inside the lens domain. The effect of mode conversion on the performance of the lens is analyzed in Fig. 2 by comparing the focusing power of cube-

and sphere-shaped lenses made of PLA to lenses made of a material with P-wave speed matched to water ($c_p = c_w$) and much lower S-wave speed ($c_s = 700$ m/s), i.e., softer material. Overall a soft lens with P-wave speed matched to water outperforms a lens made of PLA; however, PLA and similar stiff polymer materials are more practically used as filaments in FDM 3D printers. For the matched material, the shape of the lens had a limited effect on its performance as shown by comparing the solid blue curves in Figs. 2(a) and 2(e), as well as Figs. 2(c) and 2(g). However, when PLA is considered, the shape of the lens has a strong effect on the focal spot size as shown by comparing Figs. 2(d) and 2(h). The focal spot size (i.e., neck of the focus) is much larger for the cube-shaped lens even though the pressure amplitude is comparable in both cases. This indicates that a spatially wider high-pressure region is enabled by the cube PLA lens compared to its spherical counterpart. The effect of varying the direction of incident plane waves is also considered in Figs. 2(e) and 2(f). Plane waves propagating in the $\Gamma X \langle 100 \rangle$ direction of the lattice are compared to waves propagating in the $\Gamma R \langle 111 \rangle$ direction. For the matched lens, the direction has a limited effect on the lens performance, i.e., the lens retains the omnidirectional characteristics of Luneburg lens. For PLA on the other hand, the performance of the lens deteriorates in the $\langle 111 \rangle$ direction. Since PLA has c_p greater than water, larger filling fractions are required to realize the Luneburg profile, as shown in the insets of Fig. 2(a). The larger filling fraction introduces larger anisotropy in c_p, which causes the lens profile to change
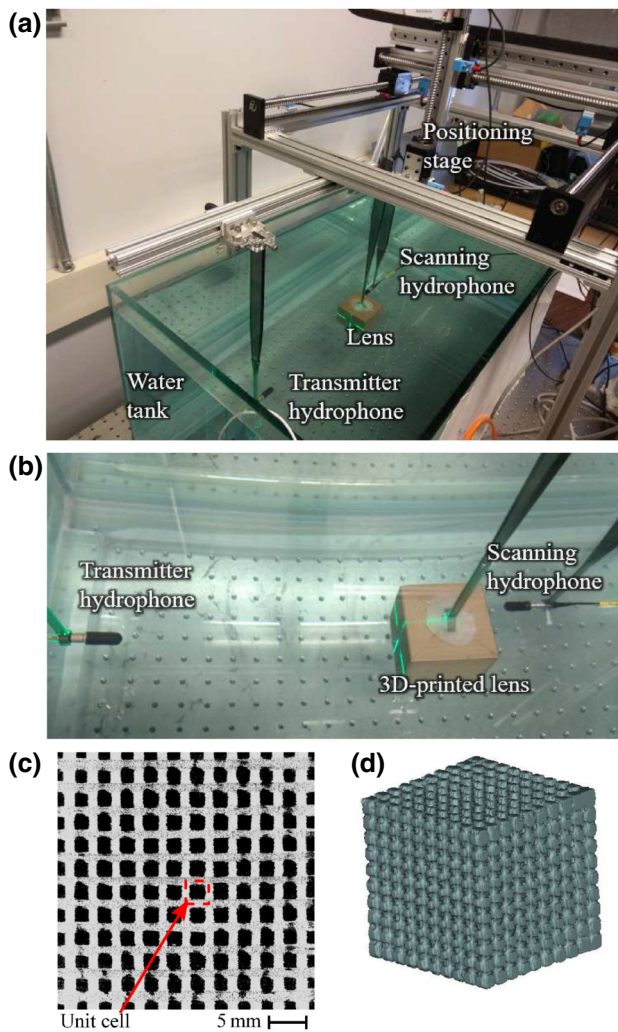
FIG. 3. (a) Overview and (b) close-up view of the experimental setup for plane-wave generation and for scanning the pressure field behind the 3D-printed PC lens. (c) X-ray scan of the internal structure at the midsection of the 3D-printed lens. (d) 3D reconstruction of an x-ray scan of the inner ten cells of the lens.

depending on the direction of incidence. This anisotropy, however, could be reduced by considering a more complex lattice structure [36] ideally, which would bring fabrication challenges as a compromise.

IV. EXPERIMENTAL VALIDATION

To validate the numerical results in underwater experiments [Figs. 3(a) and 3(b)], a proof-of-concept cube-shaped PLA lens is fabricated using a desktop 3D printer (Ultimaker 3), with standard printing parameters, and a printing layer height of 0.2 mm. The lens consists of $16 \times 16 \times 16$ (4096) unit cells with a lattice parameter of 3 mm, yielding the overall dimensions of $48.8 \times 48.8 \times 48.8$ mm^3. It is designed to achieve focusing around a target frequency of 100 kHz. The external surface of the
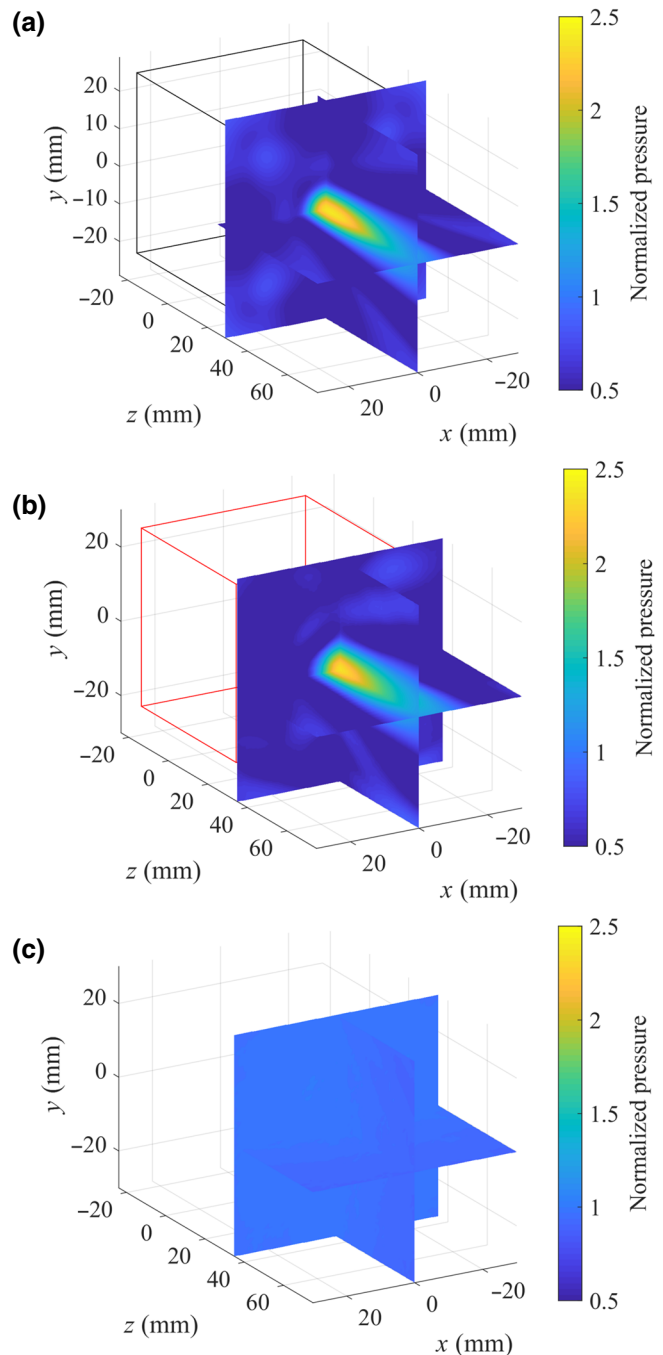

FIG. 4. Peak pressure field behind the lens (focus region) revealing a substantial enhancement of the pressure intensity via focusing. (a) Numerical (FEM) simulation, (b) experimental data (via scanning using the hydrophone), and (c) baseline case without the lens (obtained from experiments).

lens is sealed with a subwavelength 0.4-mm wall of 3D-printed PLA to avoid any leakage. The internal structure of the fabricated lens is scanned using a Scanco uCT50 microcomputed tomography (micro-CT) x-ray imaging system. Figures 3(c) and 3(d) show the internal structure of the lens with the gradient variation of the air-inclusion size.

The corners of the cubic structure are rounded to a radius of approximately 0.5 mm, which is expected since sharp corners are hard to realize using common 3D-printing techniques. Some small voids are also observed in the PLA domain, which is another limitation of the FDM-printing technique used. Nevertheless, since the unit cell is much smaller than the incident wavelength ($a = 0.2\lambda$ where $\lambda = 15$ mm is the wavelength in water at 100 kHz), minor defects are expected to have a limited effect on the overall performance of the device.

The pressure field behind the lens (in the focus region) is mapped experimentally by mounting the lens inside a water tank with a scanning hydrophone setup as shown in Figs. 3(a) and 3(b). A hydrophone (B&K 8103) is used as a spherical point source transmitter to enable plane waves in its far field. The distance between the transmitter and the center of the lens is set to 280 mm (18.6λ) to ensure sufficient distance for plane-wave formation. Another receiver hydrophone (RESON TC 4013) is mounted on a precision stage for accurate 3D positioning. The acoustic center of the hydrophone is located 10 mm from its tip, which limits the minimum distance for measuring the pressure field from the surface of the lens to this distance. The transmitter hydrophone is excited with a 30-kHz bandwidth Gaussian pulse centered at 100 kHz using an arbitrary signal generator (HP 33120A) and a piezoelectric amplifier (Khron-Hite 7500). The receiving hydrophone is used to scan the pressure field behind the lens by connecting it through a preamplifier (Stanford Research Systems SR560) to a digital oscilloscope (HandyScope HS3). The control of the stage, excitation signal, and the data acquisition are integrated into a single Labview program on a laptop, which is connected to both the oscilloscope and the signal generator.

The lens is excited with a plane wave traveling in the positive z direction, and the peak of the pressure field behind the lens is plotted in Fig. 4 for three perpendicular measurement planes. The pressure field obtained experimentally [shown in Fig. 4(a)] is in excellent agreement with that obtained numerically [shown in Fig. 4(b)]. A clear 3D wave focusing is observed by comparing the experimental and numerical results to the baseline experimental pressure field without the presence of the lens [shown in Fig. 4(c)]. The pressure fields at the focal plane along the x direction as well as along the propagation direction (z direction) are shown in Fig. 5. The experimental and numerical results are in excellent agreement especially near the focal point. The inhomogeneities observed in the microstructure of the printed lens [Fig. 3(c)] has little effect on the performance of the lens, which is expected since their dimensions are much smaller than the wavelength at the target frequency. It should be noted that accurate identification of material properties of the printed material is important for designing the structure of the lens as well as getting good agreement between experimental results
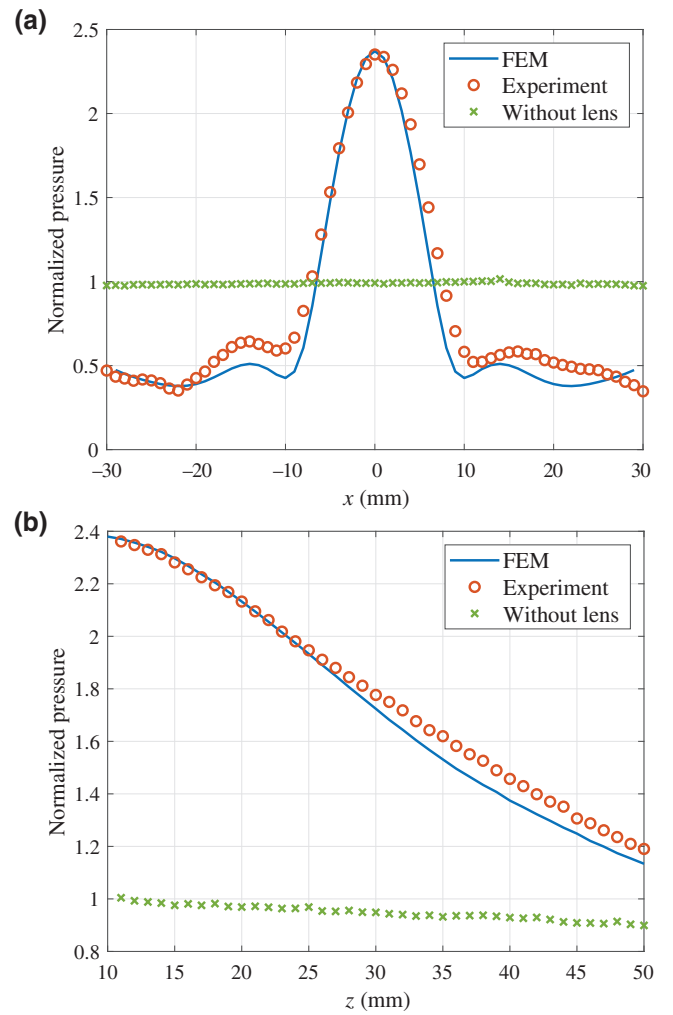

FIG. 5. Comparison of the experimental and numerical pressure distributions along the (a) x axis of the focal plane normal to the propagation direction, and along (b) the z axis (in the propagation direction). The baseline case without the lens is also shown for reference.

and numerical predictions. A peak amplification factor of 2.38 is observed experimentally, which corresponds to a power gain of 5.7 and a 7.5-dB gain compared to the field without the presence of the lens. Higher amplitude gains are shown numerically [up to a factor of 4.25 as shown in Fig. 2(a)]; however, special filaments and 3D-printing processes might be needed to achieve this performance, since low attenuation filaments with P-wave speed close to water are required.

V. CONCLUSIONS

A simple approach to design and fabricate 3D GRIN PCs for underwater acoustic applications is introduced. The proposed concept does not require bulky or heavy inclusions to enable the required refractive-index profile.

A 3D GRIN PC lens is designed, simulated, 3D printed, and experimentally validated. The overall concept, beyond the specific lens design, may pave the way for leveraging 3D-printed GRIN PC structures to achieve power or signal enhancement in applications spanning from underwater acoustic sensing to biomedical imaging.

---

[1] Z. He, F. Cai, and Z. Liu, Guiding acoustic waves with graded phononic crystals, Solid State Commun. **148**, 74 (2008).

[2] L.-Y. Wu and L.-W. Chen, An acoustic bending waveguide designed by graded sonic crystals, J. Appl. Phys. **110**, 114507 (2011).

[3] S.-C. S. Lin, T. J. Huang, J.-H. Sun, and T.-T. Wu, Gradient-index phononic crystals, Phys. Rev. B **79**, 094302 (2009).

[4] A. Climente, D. Torrent, and J. Sánchez-Dehesa, Sound focusing by gradient index sonic lenses, Appl. Phys. Lett. **97**, 104103 (2010).

[5] T. P. Martin, M. Nicholas, G. J. Orris, L.-W. Cai, D. Torrent, and J. Sánchez-Dehesa, Sonic gradient index lens for aqueous applications, Appl. Phys. Lett. **97**, 113503 (2010).

[6] L. Zigoneanu, B.-I. Popa, and S. A. Cummer, Design and measurements of a broadband two-dimensional acoustic lens, Phys. Rev. B **84**, 024305 (2011).

[7] Y. Li, G. Yu, B. Liang, X. Zou, G. Li, S. Cheng, and J. Cheng, Three-dimensional ultrathin planar lenses by acoustic metamaterials, Sci. Rep. **4**, 6830 (2014).

[8] A. Climente, D. Torrent, and J. Sánchez-Dehesa, Gradient index lenses for flexural waves based on thickness variations, Appl. Phys. Lett. **105**, 064101 (2014).

[9] J. Zhao, B. Bonello, R. Marchal, and O. Boyko, Beam path and focusing of flexural Lamb waves within phononic crystal-based acoustic lenses, New J. Phys. **16**, 063031 (2014).

[10] Y. Chen, H. Liu, M. Reilly, H. Bae, and M. Yu, Enhanced acoustic sensing through wave compression and pressure amplification in anisotropic metamaterials, Nat. Commun. **5**, 5247 (2014).

[11] Y.-J. Liang, L.-W. Chen, C.-C. Wang, and I.-L. Chang, An acoustic absorber implemented by graded index phononic crystals, J. Appl. Phys. **115**, 244513 (2014).

[12] N. Jiménez, V. Romero-García, A. Cebrecos, R. Picó, V. J. Sánchez-Morcillo, and L. M. Garcia-Raffi, Broadband quasi perfect absorption using chirped multi-layer porous materials, AIP Adv. **6**, 121605 (2016).

[13] X. H. Zhang, Z. G. Qu, X. C. He, and D. L. Lu, Experimental study on the sound absorption characteristics of continuously graded phononic crystals, AIP Adv. **6**, 105205 (2016).

[14] R. Fleury and A. Alù, Metamaterial buffer for broadband non-resonant impedance matching of obliquely incident acoustic waves, J. Acoust. Soc. Am. **136**, 2935 (2014).

[15] Y. Fu, J. Li, Y. Xie, C. Shen, Y. Xu, H. Chen, and S. A. Cummer, Compact acoustic retroreflector based on a mirrored Luneburg lens, Phys. Rev. Mater. **2**, 105202 (2018).

[16] C. J. Naify, T. P. Martin, C. N. Layman, M. Nicholas, A. L. Thangawng, D. C. Calvo, and G. J. Orris, Underwater acoustic omnidirectional absorber, Appl. Phys. Lett. **104**, 073505 (2014).

[17] F. Ju, Y. Tian, Y. Cheng, and X. Liu, Asymmetric acoustic transmission with a lossy gradient-index metasurface, Appl. Phys. Lett. **113**, 121901 (2018).

[18] S. Tol, F. L. Degertekin, and A. Erturk, Gradient-index phononic crystal lens-based enhancement of elastic wave energy harvesting, Appl. Phys. Lett. **109**, 063902 (2016).

[19] S. Tol, F. L. Degertekin, and A. Erturk, Phononic crystal Luneburg lens for omnidirectional elastic wave focusing and energy harvesting, Appl. Phys. Lett. **111**, 013503 (2017).

[20] J. Zhao, B. Bonello, L. Becerra, O. Boyko, and R. Marchal, Focusing of Rayleigh waves with gradient-index phononic crystals, Appl. Phys. Lett. **108**, 221905 (2016).

[21] A. Colombi, V. Ageeva, R. J. Smith, A. Clare, R. Patel, M. Clark, D. Colquitt, P. Roux, S. Guenneau, and R. V. Craster, Enhanced sensing and conversion of ultrasonic Rayleigh waves by elastic metasurfaces, Sci. Rep. **7**, 6750 (2017).

[22] H. Y. Dong, Q. Cheng, G. Y. Song, W. X. Tang, J. Wang, and T. J. Cui, Realization of broadband acoustic metamaterial lens with quasi-conformal mapping, Appl. Phys. Express **10**, 087202 (2017).

[23] X. Su, A. N. Norris, C. W. Cushing, M. R. Haberman, and P. S. Wilson, Broadband focusing of underwater sound using a transparent pentamode lens, J. Acoust. Soc. Am. **141**, 4408 (2017).

[24] R. Zhu, C. Ma, B. Zheng, M. Y. Musa, L. Jing, Y. Yang, H. Wang, S. Dehdashti, N. X. Fang, and H. Chen, Bifunctional acoustic metamaterial lens designed with coordinate transformation, Appl. Phys. Lett. **110**, 113503 (2017).

[25] C. M. Park and S. H. Lee, Acoustic Luneburg lens using orifice-type metamaterial unit cells, Appl. Phys. Lett. **112**, 074101 (2018).

[26] Y. Jin, R. Kumar, O. Poncelet, O. Mondain-Monval, and T. Brunet, Flat acoustics with soft gradient-index metasurfaces, Nat. Commun. **10**, 143 (2019).

[27] Y. Ruan, X. Liang, Z. Wang, T. Wang, Y. Deng, F. Qu, and J. Zhang, 3-D underwater acoustic wave focusing by periodic structure, Appl. Phys. Lett. **114**, 081908 (2019).

[28] A. Sukhovich, L. Jing, and J. H. Page, Negative refraction and focusing of ultrasound in two-dimensional phononic crystals, Phys. Rev. B **77**, 014301 (2008).

[29] G. D'Aguanno, K. Q. Le, R. Trimm, A. Alù, N. Mattiucci, A. D. Mathias, N. Aközbek, and M. J. Bloemer, Broadband metamaterial for nonresonant matching of acoustic waves, Sci. Rep. **2**, 340 (2012).

[30] A. Hladky-Hennion, C. Croenne, J. O. Vasseur, L. Haumesser, and A. N. Norris, Focusing capability of a phononic crystal based on a hollow metallic structure, IEEE Trans. Ultrason., Ferroelectr., Freq. Control **61**, 1314 (2014).

[31] T. P. Martin, C. J. Naify, E. A. Skerritt, C. N. Layman, M. Nicholas, D. C. Calvo, G. J. Orris, D. Torrent, and J. Sánchez-Dehesa, Transparent Gradient-Index Lens for Underwater Sound Based on Phase Advance, Phys. Rev. Appl. **4**, 034003 (2015).

[32] S. A. M. Tofail, E. P. Koumoulos, A. Bandyopadhyay, S. Bose, L. O'Donoghue, and C. Charitidis, Additive manufacturing: Scientific and technological challenges, market uptake and opportunities, Mater. Today **21**, 22 (2018).

[33] Y. Xie, Y. Fu, Z. Jia, J. Li, C. Shen, Y. Xu, H. Chen, and S. A. Cummer, Acoustic imaging with metamaterial Luneburg lenses, Sci. Rep. **8**, 16188 (2018).

[34] N. Guo and M. C. Leu, Additive manufacturing: Technology, applications and research needs, Front. Mech. Eng. **8**, 215 (2013).

[35] F. M. Guillot and D. H. Trivett, Complete elastic characterization of viscoelastic materials by dynamic measurements of the complex bulk and Young's moduli as a function of temperature and hydrostatic pressure, J. Sound Vib. **330**, 3334 (2011).

[36] T. Tancogne-Dejean, M. Diamantopoulou, M. B. Gorji, C. Bonatti, and D. Mohr, 3D plate-lattices: An emerging class of low-density metamaterial exhibiting optimal isotropic stiffness, Adv. Mater. **30**, 1803334 (2018).